Klein Tunneling in the presence of random impurities

S. Palpacelli,[1, *] M. Mendoza,[2, †] H. J. Herrmann,[2, ‡] and S. Succi[3, §]

[1] *Numidia s.r.l., Via Giacomo Peroni, 130, 00131, Roma, Italy.*
[2] *ETH Zürich, Computational Physics for Engineering Materials,*
Institute for Building Materials, Schafmattstrasse 6, HIF, CH-8093 Zürich, Switzerland.
[3] *Istituto per le Applicazioni del Calcolo C.N.R., Via dei Taurini, 19 00185, Rome Italy,*
and Freiburg Institute for Advanced Studies, Albertstrasse, 19, D-79104, Freiburg, Germany.
(Dated: February 28, 2012)

In this paper, we study Klein tunneling in random media. To this purpose, we simulate the propagation of a relativistic Gaussian wavepacket through a graphene sample with randomly distributed potential barriers (impurities). The simulations, based on a relativistic quantum lattice Boltzmann method, permit to compute the transmission coefficient across the sample, thereby providing an estimate for the conductivity as a function of impurity concentration and strength of the potentials. It is found that the conductivity loss due to impurities is significantly higher for wave-packets of massive particles, as compared to massless ones. A general expression for the loss of conductivity as a function of the impurity percentage is presented and successfully compared with the Kozeny-Carman law for disordered media in classical fluid dynamics.

I. INTRODUCTION

As opposed to classical quantum mechanics where electrons tunneling into a barrier are exponentially damped, relativistic scattering was shown by Klein in 1929[1] to follow a very unexpected behavior: If the potential is of the order of the electron mass or higher the barrier becomes virtually transparent to the electrons. This is called the Klein paradox. Experimental realizations were not available until the recent discovery of graphene[2,3]. This material has revealed a series of amazing properties, such as ultra-high electrical conductivity, ultra-low shear viscosity to entropy ratio, as well as exceptional structural strength, as combined with mechanical flexibility and optical transparency. Many of these fascinating properties are due to the fact that, consisting of literally one single carbon monolayer, graphene represents the first instance ever of a truly two-dimensional material (the "ultimate flatland"[4]). Moreover, due to the special symmetries of the honeycomb lattice, electrons in graphene are shown to behave like an effective Dirac fluid of *massless* chiral quasi-particles, propagating at a Fermi speed of about $v_F \sim c/300 \sim 10^6$ m/s. This configures graphene as an unique, slow-relativistic electronic fluid, where many unexpected quantum-electrodynamic phenomena can take place[5]. For instance, since electrons are about 300 times slower than photons, their mutual interaction is proportionately enhanced, leading to an effective fine-structure constant $\alpha_{gr} = e^2/\hbar v_F \sim 1$. As a result of such strong interactions, it has been recently proposed that this peculiar 2D graphene electron gas should be characterized by an exceptionally low viscosity/entropy ratio (near-perfect fluid), coming close to the famous AdS-CFT lower bound conjectured for quantum-chromodynamic fluids, such as quark-gluon plasmas[5]. This spawns the exciting prospect of observing electronic pre-turbulence in graphene samples, as first pointed out in Ref.[6] and confirmed by recent numerical simulations[7].

The zero-mass of electronic excitations in graphene may have other spectacular consequences. For instance, it has been recently pointed out[8] that graphene could offer the first experimental of the so-called Klein paradox, i.e. the capability of quantum wavefunctions to undergo zero reflection from a potential barrier much higher than the energy of the wavefunction itself. This property, which relies exclusively upon the spinorial nature of the Dirac wavefunction, stands in stark contrast with the corresponding non-relativistic behavior, which predicts an exponential decay of the transmission coefficient with the difference $V_0 - E$, V_0 being the height of the barrier and E the wavefunction energy. Based on an analytical solution of the scattering problem for a monochromatic plane wave, the authors were able to show that, depending on a series of geometrical and energy parameters, special angles of incidence (resonant angles) provide literally zero reflectivity: the plane wave goes completely across the barrier. Besides its intellectual charm, such property is of great practical interest for the study of electronic transport in graphene[9,10], and it is expected to play an important role in the understanding of the minimum conductivity of graphene[11]. Furthermore, the electronic spectrum of graphene can change depending on the substrate, for instance on SiC the energy spectrum presents a gap of width $2mv_F^2$, which makes it possible to model the electric transport by using the massive Dirac equation[12,13]. Therefore, it is also interesting to study the Klein tunneling in a random media for this kind of gaped-samples (massive fermions case).

On the other hand, due to the fact that, under suitable conditions[6], electronic excitations in graphene behave as an effective relativistic Dirac fluid, in the presence of a random media, transport laws similar to the
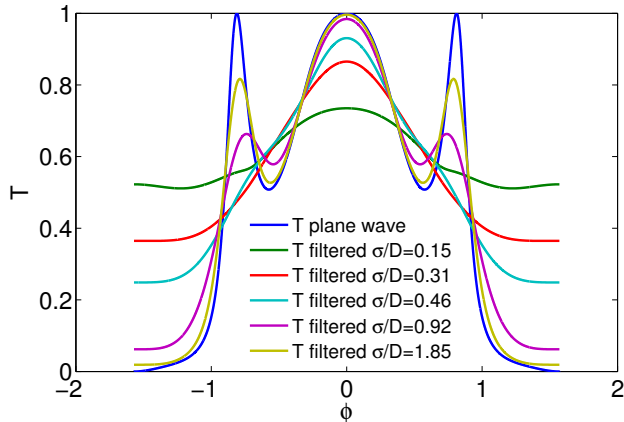
FIG. 1. The transmission coefficient of a Gaussian wavepacket, as computed with the analytical convolution, Eq. (15), as a function of the incidence angle ϕ for $\sigma/D = 0.15, 0.31, 0.46, 0.92, 1.85$. The blue line corresponds to the unfiltered case, $\sigma \to \infty$, corresponding to a plane wave.

ones ruling fluid motion in diluted porous media, may be expected to apply. We refer here, e.g. to the Carman-Kozeny law[14,15], which relates the permeability of a porous medium (conductivity of a graphene sample) to the solid concentration (impurity density).

The paper is organized as follows: first, we introduce a brief description of the quantum lattice Boltzmann (QLB) method[16]; second, we study the case of Klein tunneling of a Gaussian wave packet through a rectangular potential barrier. Subsequently, we present numerical solutions of the Dirac equation in the presence of random impurities, thereby providing an estimate for the effects of the impurity concentration on the conductivity of the graphene sample, for both cases, massless and massive Dirac fermions. The simulations are performed using a QLB model, which is also introduced as a new tool to study transport phenomena in graphene. Finally, we discuss and summarize the results.

II. THE QUANTUM LATTICE BOLTZMANN METHOD

The quantum lattice Boltzmann (QLB) method[16] is a quantum-kinetic technique that was originally devised for non-relativistic quantum problems and recently shown to provide a second-order accurate solver for relativistic wave scattering and propagation[17]. Since the method is relatively new in the relativistic context, for the sake of self-containedness, we revisit here its main technical aspects. For full details, see our recent work[18,19].

The quantum lattice Boltzmann equation was initially derived from a formal parallel between the kinetic lattice Boltzmann equation and the single-particle Dirac equation[16,20,21]. For our purpose, it proves expedient to transform the standard form of the Dirac equation into
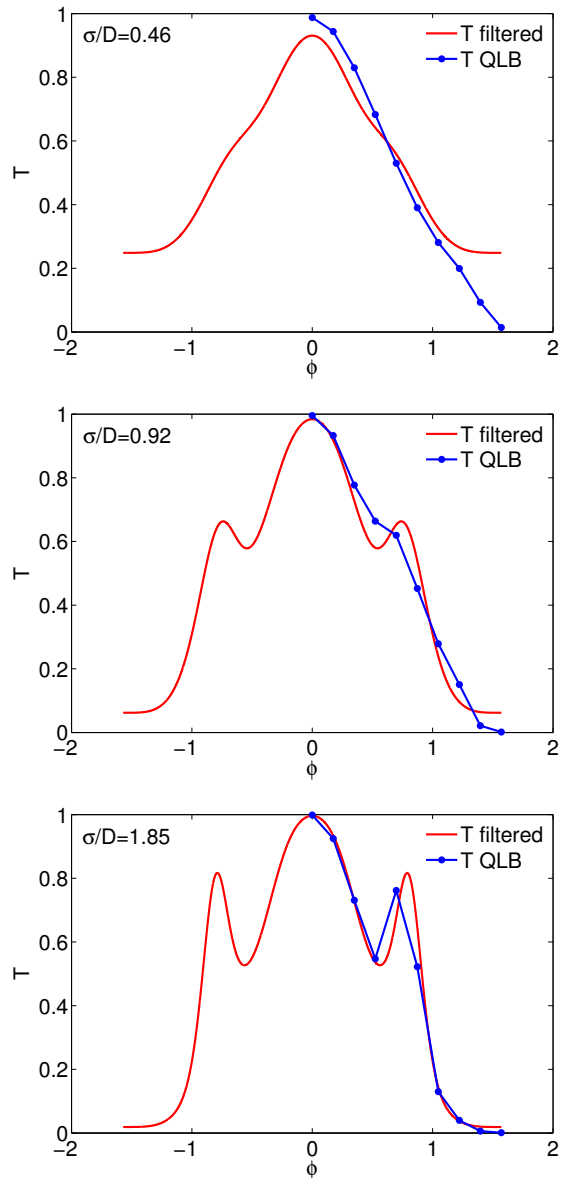

FIG. 2. The transmission coefficient of a Gaussian wavepacket as a function of the incidence angle ϕ for $\sigma = 24, 48$ and 96 (in lattice units), corresponding to $\sigma/D = 0.46, 0.92, 1.85$, as computed via convolution (solid line) and by QLB simulations (line with dots).

the Majorana form, in which all matrices are real[22],

$$[\partial_t + c(-\alpha^x \partial_x + \beta \partial_y - \alpha^z \partial_z) + i\omega_c \alpha^y - igI]\psi = 0, \quad (1)$$

This form is obtained by multiplying the standard Dirac equation on the left and right by the involution matrix $U = 2^{-1/2}(\alpha^y + \beta)$. In the above, c is the light speed, $\hbar$ is the reduced Planck's constant, I is the identity operator, and $\omega_c = mc^2/\hbar$ is the Compton frequency for a particle of mass m. The wavefunction ψ is a complex four-spinor, and α and β are the standard Dirac matrices. The last term couples the wavefunction to an applied scalar poten-
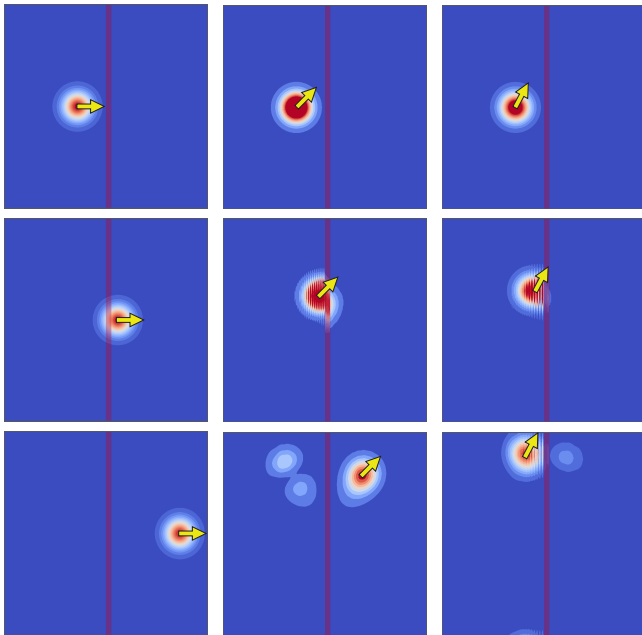
FIG. 3. Snapshots of the wavepacket density at various instants, $t = 0, 420, 1050$ (lattice units), for the case $\phi = 0$ (left) and $\phi = 2\pi/9$ (middle), and $\phi = \pi/3$ (right) for $\sigma/D = 1.85$. In the middle, as one can see, after significant distortion in the intermediate stage of the evolution, the wavepacket manages to be transmitted across the barrier to a substantial extent ($T = 0.76$). On the other hand, at the right, the packet is mostly bounced-back by the barrier, with transmission coefficient as low as $T = 0.13$. For visualization purposes, the color bar scale has been modified independently for each figure.

tial $V(x, y, z)$ via the coefficient $g = qV/\hbar$, where q is the electric charge[22]. Note that since the spin states mix-up during propagation (spinning particles), there is no basis in which all three matrices α^x, α^y, α^z are simultaneously diagonal.

Let us consider a one-dimensional version of the Dirac equation. In particular, let Z be a unitary matrix, diagonalizing the streaming matrix $-\alpha^z$:

$$Z = \frac{1}{\sqrt{2}} \begin{pmatrix} 0 & -1 & 0 & 1 \\ 1 & 0 & -1 & 0 \\ 0 & 1 & 0 & 1 \\ 1 & 0 & 1 & 0 \end{pmatrix}. \tag{2}$$

Applying the matrix Z to Eq. (1), the streaming matrix along z is diagonalized and the collision matrix is also transformed accordingly

$$\big[\partial_t + cZ^{-1}(-\alpha^z)Z\partial_z \\ + Z^{-1}(-c\alpha^x\partial_x + c\beta\partial_y + i\omega_c\alpha^y - igI)Z \big] Z^{-1}\psi = 0. \tag{3}$$

Neglecting any dependence of ψ on the x and y coordinates, Eq. (3) may be written as a pair of one-dimensional Dirac equations

$$\partial_t u_{1,2} + c\partial_z u_{1,2} = \omega_c d_{2,1} + igu_{1,2}, \\ \partial_t d_{1,2} - c\partial_z d_{1,2} = -\omega_c u_{2,1} + igd_{1,2}, \tag{4}$$

for the variables (u_1, d_2) and (u_2, d_1) that represent the rotated wavefunction $Z^{-1}\psi = (u_1, u_2, d_1, d_2)^T$. The components u and d propagate up and down the z axis respectively, and the subscripts indicate the spin up (1) and spin down (2) states, respectively. The system of Eq. (4) may be treated as a Boltzmann equation for a pair of complex distribution functions $u_{1,2}$ and $d_{1,2}$[16]. Equation (4) may thus be discretized using the same approach as in lattice Boltzmann method, i.e. by integrating along the characteristic light-cones $dz = \pm cdt$.

The resulting system of algebraic equations reads as follows

$$\widehat{u}_{1,2} - u_{1,2} = \frac{1}{2}\widetilde{m}(d_{2,1} + \widehat{d}_{2,1}) + \frac{1}{2}i\widetilde{g}(u_{1,2} + \widehat{u}_{1,2}), \\ \widehat{d}_{1,2} - d_{1,2} = -\frac{1}{2}\widetilde{m}(u_{2,1} + \widehat{u}_{2,1}) + \frac{1}{2}i\widetilde{g}(d_{1,2} + \widehat{d}_{1,2}), \tag{5}$$

where the hat superscript (^) indicates that the wavefunction is evaluated at the end-point of the corresponding streaming step, namely

$$\widehat{u}_{1,2} = u_{1,2}(z + \Delta z, t + \Delta t), \quad u_{1,2} = u_{1,2}(z, t) \\ \widehat{d}_{1,2} = d_{1,2}(z - \Delta z, t + \Delta t), \quad d_{1,2} = d_{1,2}(z, t). \tag{6}$$

The dimensionless Compton frequency is $\widetilde{m} = \omega_c \Delta t$, and the dimensionless scalar potential is $\widetilde{g} = g(z, t)\Delta t$.

The pair of equations (5) can be solved algebraically, delivering explicit expressions for $\widehat{u}_{1,2}$ and $\widehat{d}_{1,2}$:

$$\widehat{u}_{1,2} = au_{1,2} + bd_{2,1}, \\ \widehat{d}_{1,2} = ad_{1,2} - bu_{2,1}, \tag{7}$$

where the coefficients a and b are

$$a = \frac{1 - \Omega/4}{1 + \Omega/4 - i\widetilde{g}}, \quad b = \frac{\widetilde{m}}{1 + \Omega/4 - i\widetilde{g}}, \quad \Omega = \widetilde{m}^2 - \widetilde{g}^2.$$

These coefficients satisfy $|a|^2 + |b|^2 = 1$, so that the right hand side of Eq. (7) corresponds to multiplying the rotated wavefunction $Z^{-1}\psi = (u_1, u_2, d_1, d_2)^T$ by the unitary collision matrix

$$Q = \begin{pmatrix} a & 0 & 0 & b \\ 0 & a & b & 0 \\ 0 & -b & a & 0 \\ -b & 0 & 0 & a \end{pmatrix}. \tag{8}$$

The streaming step propagates $u_{1,2}$ upwards and $d_{1,2}$ downwards, along the light cones given by $\Delta z = \pm c\Delta t$. Note that this unitary operation is numerically *exact*, without round-off error, because the distribution function is integrally transferred from the source to the destination site, and no fractional transport is involved. Since both streaming and collisions step are unitary, the overall QLB scheme evolves the discrete wavefunction through a sequence of unitary operations for any value of the discrete time step Δt. In addition, since streaming proceeds upwind only (no centered spatial differences) along

the discrete light-cones associated with each component Ψ_i , the QLB dispersion relation is automatically free from fermion-doubling,[23]. This, together with the excellent efficiency of the method, especially on parallel computers[24], should make QLB a potentially appealing candidate for computational studies of electron transport in graphene.

The scheme extends to multiple dimensions through an operator splitting technique. Within this method, the three-dimensional Dirac equation splits into the sum of three one-dimensional equations, each involving spatial derivatives along one single direction. Each of the three stages representing evolution by a timestep dt is accomplished by rotating ψ to diagonalise the relevant streaming matrix, taking one timestep of the existing one-dimensional QLB scheme described above, and rotating ψ back to its original basis. The algorithm is thus composed of the following three steps: 1) Rotate ψ with X^{-1}, collide with $X^{-1}\widehat{Q}X$, stream along x, rotate back with X; 2) Rotate ψ with Y^{-1}, collide with $Y^{-1}\widehat{Q}Y$, stream along y, rotate back with Y; 3) Rotate ψ with Z^{-1}, collide with $Z^{-1}\widehat{Q}Z$, stream along z, rotate back with Z. This form emphasizes the symmetry between the three steps, but since the streaming matrix along y is already diagonal in the Majorana form, $Y = I$ is the identity matrix. The matrix X reads as follows:

$$X = \frac{1}{\sqrt{2}} \begin{pmatrix} -1 & 0 & 1 & 0 \\ 0 & 1 & 0 & -1 \\ 1 & 0 & 1 & 0 \\ 0 & 1 & 0 & 1 \end{pmatrix}, \quad (9)$$

and the Z matrix is given in Eq. (2) above.

The collision term splits into three parts, each of which is combined with the corresponding streaming step. The collision matrix thus coincides, up to a unitary transformation, with the collision matrix for the one-dimensional QLB scheme, with a timestep $\frac{1}{3}dt$ (see Ref.[19]). In particular, $\widehat{Q}$ is given by

$$\widehat{Q} = \begin{pmatrix} \widehat{a} & 0 & 0 & -\widehat{b} \\ 0 & \widehat{a} & \widehat{b} & 0 \\ 0 & -\widehat{b} & \widehat{a} & 0 \\ \widehat{b} & 0 & 0 & \widehat{a} \end{pmatrix}, \quad (10)$$

where the coefficients

$$\widehat{a} = \frac{1 - \Omega_3/4}{1 + \Omega_3/4 - i\widetilde{g}_3}, \quad \widehat{b} = \frac{\widetilde{m}_3}{1 + \Omega_3/4 - i\widetilde{g}_3},$$

are written in terms of the rescaled dimensionless Compton and potential frequencies

$$\Omega_3 = \widetilde{m}_3^2 - \widetilde{g}_3^2, \quad \widetilde{m}_3 = \frac{1}{3}\omega_c dt, \quad \widetilde{g}_3 = \frac{1}{3}g dt.$$

The pattern of $+$ and $-$ signs in the $\widehat{b}$ terms on the off-diagonal of $\widehat{Q}$ follows the same pattern as the α^y matrix.

FIG. 4. Sketch of the domain setting used in our simulations of the propagation of a Gaussian wave packet through a porous medium.

The rotated matrices $X^{-1}\widehat{Q}X$ and $Z^{-1}\widehat{Q}Z$ have the same sign pattern as Q, but $\widehat{Q}$ does not.

Summarizing, QLB provides a unitary, explicit algorithm for quantum wavefunctions in which information propagates along classical trajectories represented by a sequence of three one-dimensional light-cones, thereby avoiding any mixing of the spinorial components during the streaming step. Although detailed comparisons with other techniques remain to be developed, there are reasons to believe that such simplification may result in enhanced computational efficiency, especially with parallel computers in mind. Finally, we wish to point out that the same algorithm describes both relativistic and non-relativistic quantum wavepackets, depending on the value of the mass m and the characteristic strength of the potential energy.

III. RELATIVISTIC GAUSSIAN WAVEPACKETS

Since we are interested in applications on graphene, hereafter, our simulations will be performed in two spatial dimensions, (for more details see Ref.[19]). The propagation of a plane wave through a rectangular potential barrier was discussed in Ref.[8]. However due to the fact that it only applies to monochromatic plane waves, i.e. infinitely extended states which may not necessarily be realized under all experimental conditions , it is of interest to explore to what extent are such results affected by the finite extent of the wavefunction. Here, for simplicity, we consider a Gaussian wavepacket of the form

$$\psi_l(x,y) = \frac{A_k}{(4\pi\sigma^2)^{1/2}} e^{-\frac{r^2}{4\sigma^2}} e^{i(k_x x + k_y y)}, \quad l = 1,2 \quad (11)$$

where $r^2 = x^2 + y^2$, $A_1 = 1/A$, $A_2 = e^{i\phi}/A$ with $A = \sqrt{A_1^2 + A_2^2}$. The rectangular box potential of height V_0 and width D is defined as follows:

$$V(x) = \begin{cases} V_0, & \text{if } 0 < x < D, \\ 0, & \text{elsewhere.} \end{cases} \quad (12)$$

Given the linearity of the Dirac equation and the fact that wavepackets are constituted by a Gaussian superposition of plane waves, it is natural to express the transmission coefficient of a Gaussian wavepacket of size σ

through the following convolution:

$$T_\sigma(k_x, k_y) = \int_{S_f} G\left(\frac{\vec{k} - \vec{k}'}{\sigma_k}\right) T(k'_x, k'_y) dk'_x dk'_y \quad (13)$$

where $S_f = \pi k_F^2$, with $k_F^2 = k_x^2 + k_y^2$, denotes the Fermi area, and G a Gaussian kernel of width $\sigma_k = 1/\sigma$ in mometum space. The function $T(k_x, k_y)$ is the transmission coefficient of a plane wave with vector $\vec{k} \equiv (k_x, k_y)$, which according to Ref. [8], can be calculated as $T = 1 - |r|^2$ with

$$r = \frac{2ie^{i\phi}(ss')^{-1}\sin(q_x D)(\sin\phi - ss'\sin\theta)}{[e^{-iq_x D}\cos(\phi + \theta) + e^{iq_x D}\cos(\phi - \theta)] - 2i\sin(q_x D)}, \quad (14)$$

being ϕ the incidence angle, $q_x^2 = (E - V_0)^2/\hbar^2 v_F^2$, $\theta = tan^{-1}(k_y/q_x)$ the refraction angle, $s = \text{sign}(E)$, $s' = \text{sign}(E - V_0)$, and E the Fermi energy.

Since the transmission coefficient for a plane wave only depends on the wave number k_y, and due to the fact that the x component of the wave vector experiences a perfect transmission, as a first-order *approximation*, we perform the convolution in just one dimension, k_y, that is:

$$T_\sigma(k) = \int_{-k_F}^{k_F} G\left(\frac{k - k'}{\sigma_k}\right) T(k') dk' \quad (15)$$

where we have defined $k \equiv k_y$. By setting $k' = k + q$, and expanding $T(k + q)$ around $q = 0$ to second order, Eq. (15) delivers

$$T_\sigma(k) \sim T(k) + \frac{\sigma_k^2}{2} T''(k) + O(\sigma_k^2) \quad (16)$$

where T'' is the second derivative of T with respect to k. The above expression means that resonant peaks ($T'(k_r) = 0$, $T''(k_r) < 0$) are smoothed out whenever the filter width σ_k, is sufficiently high, or, more precisely, $\sigma_k^2 > \frac{|T''(k)|}{2T(k)}$. This smoothing is the effect of non-resonant wavenumbers. Given that $\sigma = 1/\sigma_k$, one could readily estimate the minimal width σ above which the secondary resonant peak would no longer be seen by the Gaussian wavepacket. However, the asymptotic expansion given by Eq. (16) fails to represent the actual transmission coefficient of the Gaussian wavepacket near the secondary resonant peak, the reason being that, around that peak, a second order expansion is grossly inaccurate because $\sigma^2 T'' \sim 1$ and higher orders will be even less accurate. As a result, the convolution integral, Eq. (15), needs to be computed.

A. Computing the convolution

To gain a quantitative sense of the dependence of the transmission coefficient of the Gaussian wavepacket with the spatial spread σ, we have numerically computed the
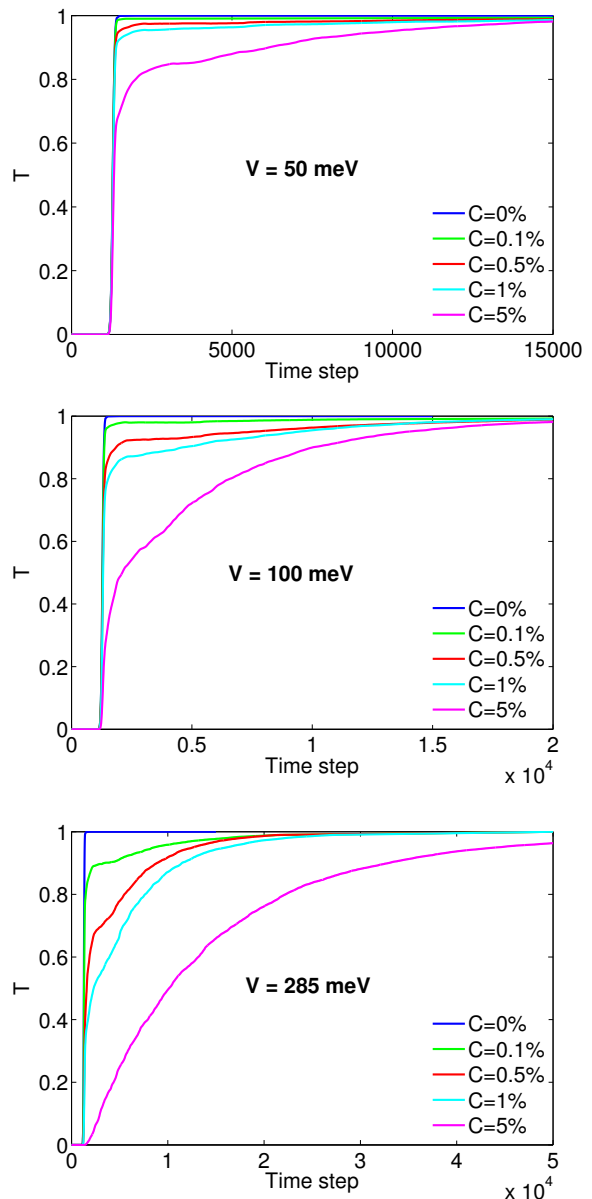

FIG. 5. Transmission coefficient as a function of time for the impurity potential set at $V = 50$, 100, and 285 meV while varying the impurity percentage C ($C = 0.1\%$, 0.5%, 1% and 5%) for $m = 0$.

convolution integral of Eq. (15), for the following values $\sigma/D = 0.15, 0.31, 0.46, 0.92, 1.85$, where $D = 100$ nm is the width of the potential barrier. The parameters are the same as in Ref.[8], namely $E = 0.08$ eV, $V_0 = 0.2$ eV and $D = 100$ nm. The results are shown in Fig.1. From this figure, it is seen that, for $\phi = 0$, $T(k_r) = T(k_F cos(\phi_r))$ goes from 1 to 0.7348, slightly over a 25 percent reduction. The same figure also shows that around the secondary resonance (at $\phi = 2\pi/9$), narrow wavepackets with $\sigma/D < 0.46$ feature $T \sim 0.5$, with no sign of the secondary resonant peak. On the other hand, the secondary peak is seen to re-emerge for $\sigma/D > 0.92$,

i.e. when σ is of the order of 100 nm, comparable with the barrier width. With $\sigma/D = 1.85$, the secondary peak is recovered, but only to about 80 percent. Note that, for $\phi = \pi/2$, the transmission coefficient is not zero, which is a consequence of the approximation made to obtain Eq. (15) from Eq. (13). However, as shown in Sec. III B, the numerical simulation of the transmission coefficient using QLB, shows generally a pretty satisfactory agreement with the approximation Eq. (15).

In order to use the plane-wave approximation, one needs to ensure that the condition $\sigma > D$ is fulfilled, which sounds pretty plausible. However, this condition is strongly dependent on the angle of incidence. In particular, it is far more stringent for oblique than for head-on ($\phi = 0$) incidence. Indeed, for $\phi = 0$, $\sigma/D \sim 0.5$ yields a substantial $T = 0.9$ for $\phi = 0$, while at $\phi = 2\pi/9$, we obtain a mere $T \sim 0.4$. At $\sigma/D \sim 2$, perfect transmission, $T = 1$, is practically recovered at $\phi = 0$, while for $\phi = 2\pi/9$, $T \sim 0.8$, i.e. about 80% percent of full transmission.

We conclude that, for head-on incidence ($\phi \sim 0$), the transmission coefficient of Gaussian packets is still similar to the one of plane waves, as soon their extent becomes comparable to the barrier width. On the other hand, the secondary resonance, at oblique incidence, is highly affected by the finite-size of the wavepacket, and full recovery of perfect transmission seems to require wavepacket extents significantly larger than the barrier width.

B. Numerical simulations

The analytical expression of Eq. (15) has been compared against direct numerical simulation of the Dirac equation, using the quantum lattice Boltzmann (QLB) method. In order to back-up the previous findings, we have computed full numerical solutions of the Dirac equation using a quantum lattice Boltzmann solver. The simulations are performed on $1024^2, 2048^2$ and 4096^2 grids, depending on the size of the Gaussian packet. Lattice units are chosen such that $\tilde{D} = D/\Delta x = 52$, $dt = dx/v_F = 1.92 \times 10^{-15}$ seconds and energy is normalized in units of $\hbar/dt$. The physical parameters are taken from Ref.[8], that is $E = 0.080$ eV, $V_0 = 0.200$ eV and $D = 100$ nm. The following sequence of wavepackets spreading, $\sigma = 24, 48, 96$ has been simulated, with $D = 52$, all in lattice units. The results of the QLB simulations appear substantially in line with the prediction of the convolution integral, i.e. they clearly show the disappearance of the secondary peak for $\sigma/D < 0.46$, and its progressive reappearance above this threshold (see Fig.2). Note that, different from the solution of the convolution integral, Eq. (15), the transmission coefficient measured by the simulation is zero for $\phi = \pi/2$, as should be expected, but the appearance of the second resonant peak is still retained.

In Fig. 3, we show typical snapshots of the wavepackets for the cases $\phi = 0$, $2\pi/9$, and $\pi/3$, for $\sigma/D = 1.85$. The snapshots clearly show that, in the case $\phi = 0$, the wavepacket crosses the barrier totally unperturbed, with literally no distortion at any stage of the evolution. In the case of oblique resonant propagation, the packet still manages to cross the barrier to a large extent, ($T = 0.76$), with significant distortions in the intermediate stages of the evolution, leaving 24 percent of the packet behind. Finally, in the case of oblique non-resonant propagation, $\phi = \pi/3$, the packet is mostly bounced-back by the barrier, with a transmission coefficient as low as $T = 0.13$.

IV. KLEIN PARADOX IN RANDOM MEDIA

One of the major technological challenges in current graphene research is to manufacture larger samples, above 10 microns, for practical use in engineering devices[25]. As the sample size is increased, however, it becomes more and more difficult to secure the purity of the sample, i.e. avoid crystalline inclusions (impurities) which alter the local structure of the graphene honeycomb lattice. Such impurities are indeed known to significantly affect the macroscopic properties of the sample, primarily its electrical conductivity. To gain insight into this problem, it is therefore of interest to investigate the propagation of relativistic wavepackets within a disordered sample.

The conductivity of two-dimensional massless fermions in disordered media has made the object of intense studies in the literature,[26]. The contribution of the present work to this subject relates to the following three directions, i) Investigate the Klein-Paradox for the case of Gaussian wave-packets rather than plane waves, both for single barriers and disordered samples, ii) Discuss the viability of semi-classical descriptions of electrons excitations in disordered media, based on quantitative analogies with flows in porous media, iii) Expose the quantum lattice Boltzmann method as a new computational tool for electron transport in graphene, which might bear a special interest for prospective implementations on parallel computers. Notwithstanding points i-iii) above, we wish to point out that, being our solution based on the single-particle Dirac equation (no many-body effects), any conclusion on transport phenomena in actual graphene samples must be taken with great caution. We also wish to remark that the Klein tunneling is expected to be relatively mild in the present set up, for two reasons. First, because the Gaussian wavepacket always includes non-resonant frequencies suffering partial reflection; second, because, being the wavepacket wider than the obstacle size (see below), it can split and turn around the obstacle like a classical fluid, hence be partially transmitted, without any quantum tunneling through the barrier.

To analyze these transport phenomena, we simulate the propagation of a relativistic Gaussian wavepacket through a two-dimensional domain composed of three regions: an inlet region, where the wave packet is positioned at the initial time $t = 0$; the impurity region,
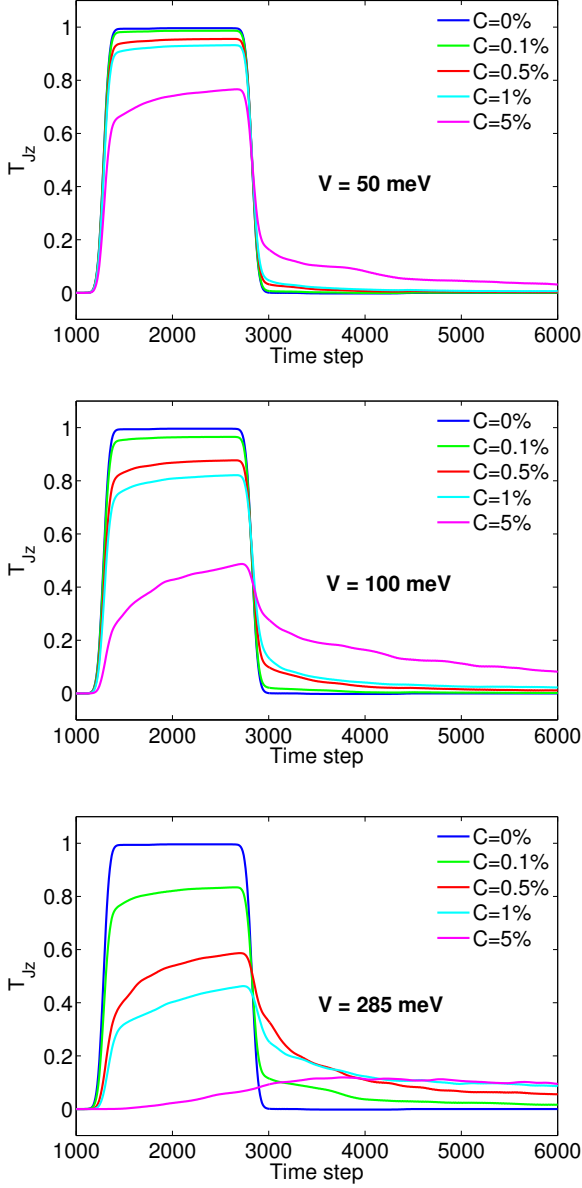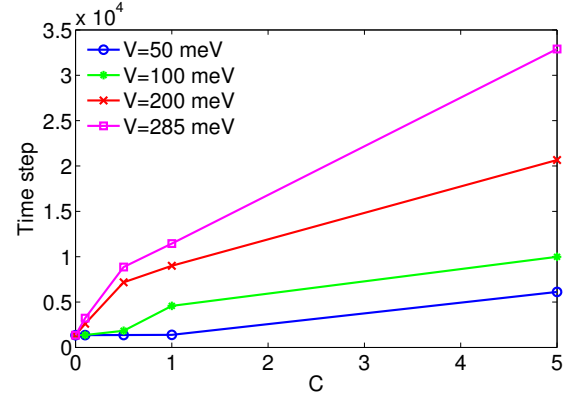
FIG. 7. Time at which 90% of the wave packet has been transmitted, $t_{0.9}$, as a function of the impurity percentage for fixed values of V and $m = 0$. The potential barriers are as follows: $V = 50, 100, 200$ and 285 meV. The impurity percentage values are $C =0.1\%, 0.5\%, 1\%$ and 5%.
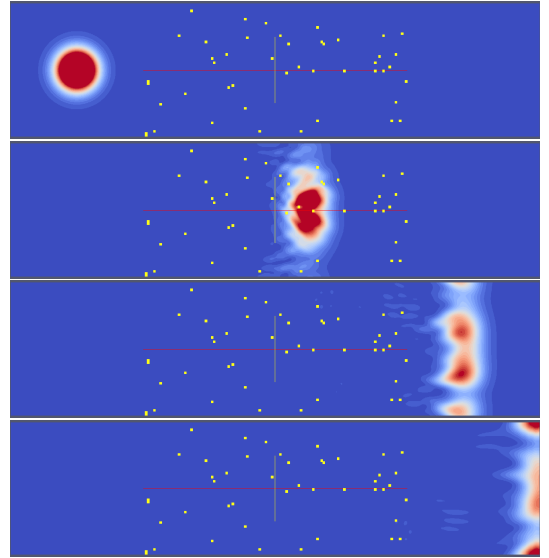

FIG. 8. Wave packet density ρ at times $= 0, 900, 1500$, and 1800 (lattice units) for the simulation performed with impurity percentage $C = 0.5\%$ and $V = 50$ meV.

FIG. 6. Momentum transmission coefficient T_{Jz} as a function of time for the impurity potential set at $V = 50, 100$, and 285 meV while varying the impurity percentage C ($C =0.1\%$, 0.5%, 1% and 5%) for $m = 0$.

i.e. the central part of the domain where randomly distributed barriers (impurities) are located; and the outlet region, which is the final region, where measurements of the transmitted wave packet are taken. Due to the large effective fine structure constant in graphene, we will neglect in our study the Coulomb interaction between carriers. The impurity concentration is given by $C = Nd^2/A$, where N is the number of square obstacles of cross section d^2, distributed over an area $A = L_y \times L_z$. For the present simulations $d = 8$ (larger than the typical lattice distante of graphene) and C is varied in the range $0.001 \div 0.05$. In Fig. 4, the computational domain is

sketched, periodic boundary conditions are imposed at top and bottom boundaries, while a bounce-back condition is enforced at the inlet , and an open boundary condition is imposed at the outlet (so that the transmitted wave packet is not reflected back). We use a square lattice of size 2048×512 cells, such that the regions $[0, 512) \times 512$, $[512, 1536) \times 512$, and $[1536, 2048] \times 512$ correspond to the inlet, impurity, and outlet regions, respectively. The cell size is chosen to be $\Delta x = 0.96$nm, and the spreading of the initial Gaussian wave packet $\sigma = 48$ (in lattice units), leading to a Fermi energy $E_F = 0.117$ (80meV in physical units). In our study, we use two values for the mass of the particles, $m = 0$ (ungaped graphene) and $m = 0.1$ (gaped graphene), and vary the impurity po-

tential and the concentration. Five barrier heights are considered, namely $V = 25, 50, 100, 200, 285$ meV. Note that, while the first two lie below E_F, hence can be overcome classically, the others can only be traversed head-on via quantum tunnelling. It should be further observed, though, that since the wavepacket is wider than the single impurity, i.e. $\sigma > d$, even in the case $E_F < V$, the wavepacket can split and turn around the obstacle like a "classical" fluid. Our results can be classified according to the energy of the particles, the potential of the barrier, and their mass as follows: weak potentials, $V < E_F - mv_F^2$; intermediate potentials, $E_F - mv_F^2 < V < E_F + mv_F^2$; and strong potentials, $V > E + mv_F^2$. The transmission coefficient $T(t)$ is obtained by computing $T(t) = \int_{z>z_{outlet}} \rho(z, y, t) dz dy$, where ρ is the wave packet density defined as $\rho = |u_1|^2 + |u_2|^2 + |d_1|^2 + |d_2|^2$, with $\psi = (u_1, u_2, d_1, d_2)^T$ being the Dirac quadrispinor.

A. Wave packet mass $m = 0$

In this first set of simulations, we fix $m = 0$, and vary the impurity concentration, C, and the strength of the impurity potential, V. In Fig. 5, we fix the value of V and we compare T while varying the impurity percentage, including the reference value for the pure sample $C = 0$. From this figure, we observe that the wave packet takes longer to regroup for high impurity concentration and high impurity potential. This is a natural consequence of the randomness induced in the wavefunction by the disordered media. However, in all cases, the complete wave packet is reconstructed after some time, with no stagnant regions left behind. This can be related to the momentum loss due to the presence of the impurities, and therefore the motion of the wave packet experiences a corresponding slow-down. Note that, in order to recover the complete wave function, the simulations have been performed in a longer domain. Otherwise the right-moving wave-packet would leave the outlet region too early while the left-mover is still in the domain. In order to provide a measurement of momentum dissipation, i.e. the loss of conductivity due to impurities, we compute the momentum transmission coefficient as follows:

$$T_{Jz}(t) = \int_{z>z_{out}} J_z(z, y, t) \quad dz dy, \qquad (17)$$

where

$$J_z = \vec{\psi}^\dagger A_z \vec{\psi} + \vec{\psi}^\dagger A_z^\dagger \vec{\psi}, \qquad (18)$$

is the z-component of the current density with A_z the streaming matrix along z and $\vec{\psi} = (u_1, u_2, d_1, d_2)^T$ the Dirac quadrispinor.

In Fig. 6, we fix the value of V and compare T_{Jz}, while varying the impurity percentage. The subscript $_{Jz}$ denotes the transmission coefficient due to the z-component of the current density, J_z. As a reference, we also plot $T_{Jz}(t)$ when the impurity percentage is set to $C = 0$.
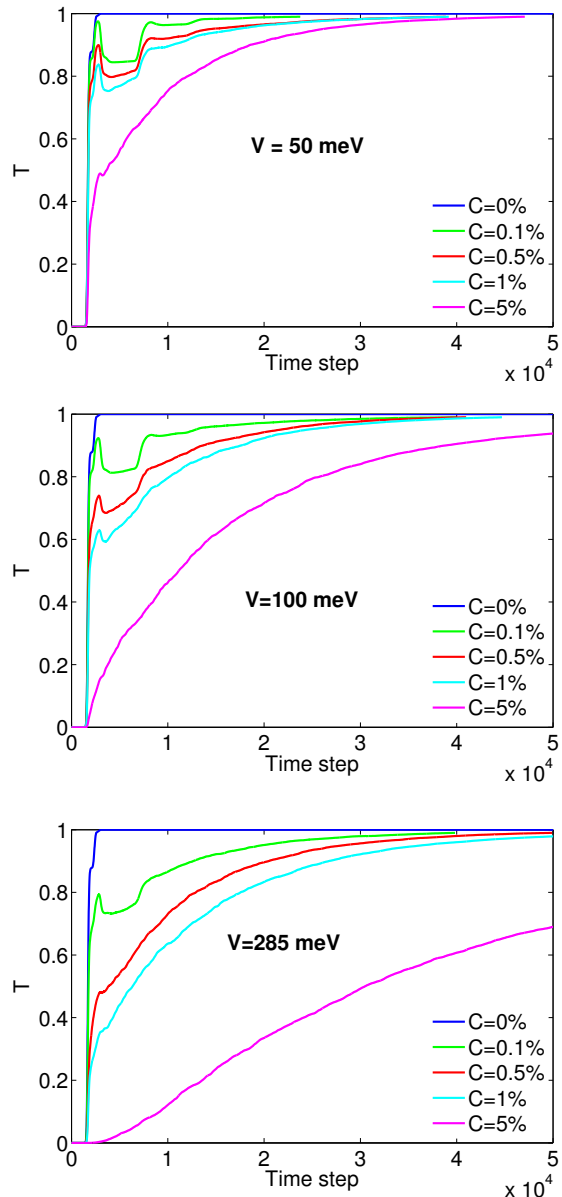

FIG. 9. Transmission coefficient as a function of time for the impurity potential set at $V = 50$, 100, and 285 meV while varying the impurity percentage ($C = 0.1\%$, 0.5%, 1% and 5%) for $m = 0.1$.

From Fig. 6 we can observe that, unlike the density, the momentum transmission coefficient does not saturate at unity (its value in the inlet region at the beginning of the simulation), because momentum is irreversibly lost in the impurity region. Furthermore, as expected, the momentum loss increases with increasing impurity potential and concentration.

As a characteristic quantity associated with the dynamics of the transmission coefficient T, in Fig. 7, we report the escape time, $t_{0.9}$, i.e. the time at which the transmission coefficient reaches 90%, (i.e. at 90% of the wave packet is transmitted through the obstacle region).
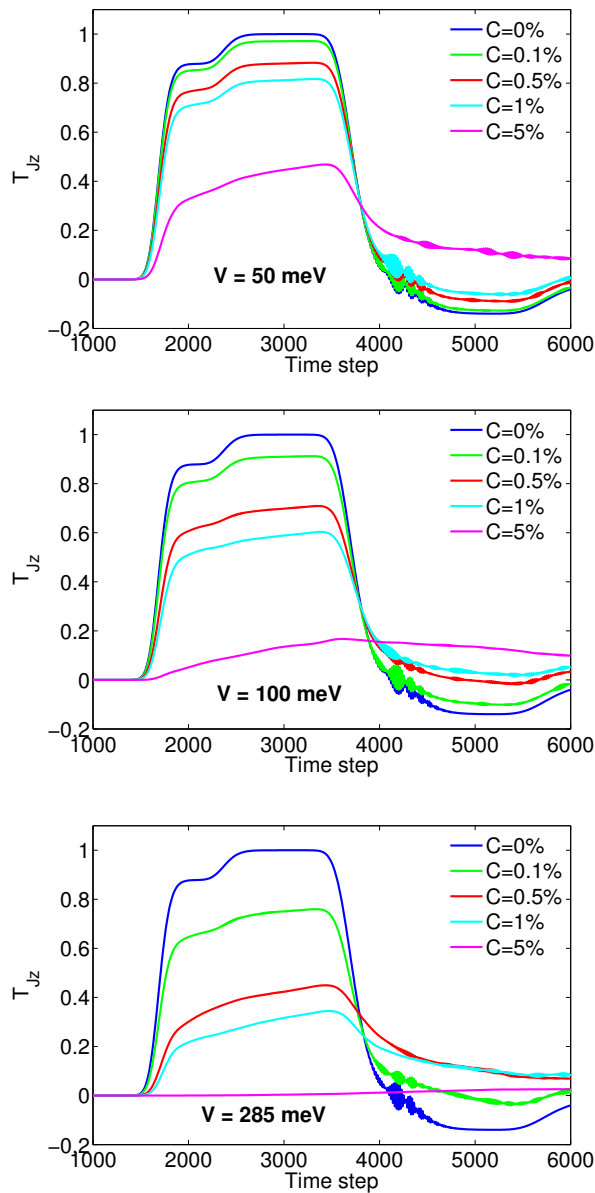
FIG. 10. Momentum transmission coefficient T_{Jz} as a function of time for the impurity potential set at $V = 50$, 100, and 285 meV while varying the impurity percentage ($C = 0.1\%$, 0.5%, 1% and 5%) for $m = 0.1$.

As above, we plot $t_{0.9}$ as a function of the impurity percentage for two values of V. We notice that for high impurity concentration the Gaussian wave packet takes longer to cross the impurity barrier. The same effect occurs when the impurity potential is increased. At low impurity concentration, $C = 0.001$, the effect of the potential barrier is relatively minor, but, as the concentration is increased, the escape time grows approximately linearly with the barrier voltage.

In Fig. 8, we show some representative snapshots of the first 1800 time steps of the simulation, for impurity percentage $C = 0.5\%$ and $V = 50$ meV. Here, we can see the
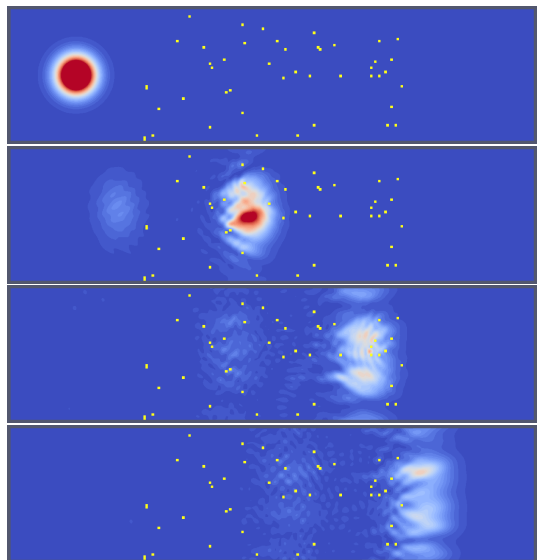

FIG. 11. Wave packet density ρ at times 0, 900, 1500, and 1800 (lattice units) for the simulation performed with impurity percentage = 0.5% and $V = 50$ meV and with $m = 0.1$.

way how the wave packet is scattered by the impurities, generating a plane front, as a result of the fragmentation of the wavefunction due to the random obstacles.

B. Wave packet mass $m = 0.1$

Next, we repeat the same simulations for the case of massive particles, with $m = 0.1$. Note that, since $mv_F^2/E_F = 0.83$, the rest energy is a significant fraction of the kinetic energy, and therefore the wavefunction comes in the form of a superposition of two wavepackets, both moving at the Fermi speed, along opposite directions, and mixing through the non-zero mass term.

In Fig. 9, we fix the value of V and compare T, while varying the impurity concentration C. As a reference, we also plot T with $C = 0$. From the results, we observe that the wave packet takes longer to cross the impurity region than for the case of $m = 0$ (the time it takes to reach a unit value of the transmission coefficient is longer). This is due the slow-down of the wavefunction as compared to the Fermi speed, because of the non-zero particle mass. Note the peak in the transmission coefficient, once the wave packet exits from the impurity region. This is due to the fact that T_{J_z} takes negative values in the late stage of the evolution, indicating the prevalence of the left-moving component of the wavepacket once the right-moving one has left the domain.

We compute the momentum transmission coefficient using equations (17) and (18). In Fig. 10, we fix the value of V and compare T_{Jz} while varying the impurity percentage. As a reference, we also plot $T_{Jz}(t)$ when the impurity percentage is set to zero. Note that, as expected, due to the inertia when the mass is increased,

the curve of the momentum transmission becomes wider than for the case of zero mass, reflecting the fact that the wave packet takes longer to move across the impurity region. In addition, the maximum momentum is smaller than for the case of zero mass, which indicates higher momentum losses. Thus, a non-zero mass of the (quasi)-particles, results in higher momentum losses. Also to be noted, are the negative values of T_{J_z} in the late stage of the evolution, indicating the presence of a left-moving component, most likely due to a spurious reflection at the outlet boundary.

In Fig. 11, we show selected snapshots from the first 1800 time steps of the simulation for impurity percentage $C = 0.5\%$ and $V = 50$ meV. From this figure, we observe that a portion of the wave packet gets "trapped", moving at lower speed, within the impurity medium, while another portion manages to move out faster.

C. Momentum Transmission Coefficient T_{Jz}

In order to summarize the results obtained in the previous sections, we inspect the maximum of the transmission coefficient T_{Jz} in Figs. 6 and 10, as a function of the impurity potential and concentration, for three different values of mass, $m = 0, 0.05, 0.1$ (see Fig. 12). These data summarize the loss of momentum, hence resistivity, due to the random impurities, formally measured by

$$\eta(C, V) = \max(T_{J_z}(C, V)) \quad . \tag{19}$$

From these figures, we observe that at high impurity concentration, $C = 0.05$, and a barrier $V = 100$ meV, the relativistic wavepacket looses about 50% of its momentum, as compared the case of a pure sample ($C = 0$). At the same concentration, a massive wave packet with $m = 0.1$, would loose more than 80%, indicating a significant drop of transmissivity due to inertia. At low impurity level, $C = 0.001$, both massless and massive wave-packets show a mild reduction of transmittivity, below 10%.

Let us now define the following "transmittance":

$$\Sigma(C, V) \equiv \frac{\eta}{1 - \eta} \quad . \tag{20}$$

This definition allows to draw a quantitative parallel with the concept of permeability of a classical fluid moving through a porous medium. That is, when the transmittance is unity, the conductivity goes formally to infinity, whereas zero transmittance connotes zero conductivity.

Using Eq. (21), we have found that the numerical results are satisfactorily fitted by the following analytical expression:

$$\Sigma(C, V) = A \frac{(1 - C)^{n+1}}{C^n} + \Sigma_0 \quad , \tag{21}$$

where A, n, Σ_0 are fitting parameters, which depend on the strength of the potential and the mass of the particles. In Fig. 12, we report the results of the fitting
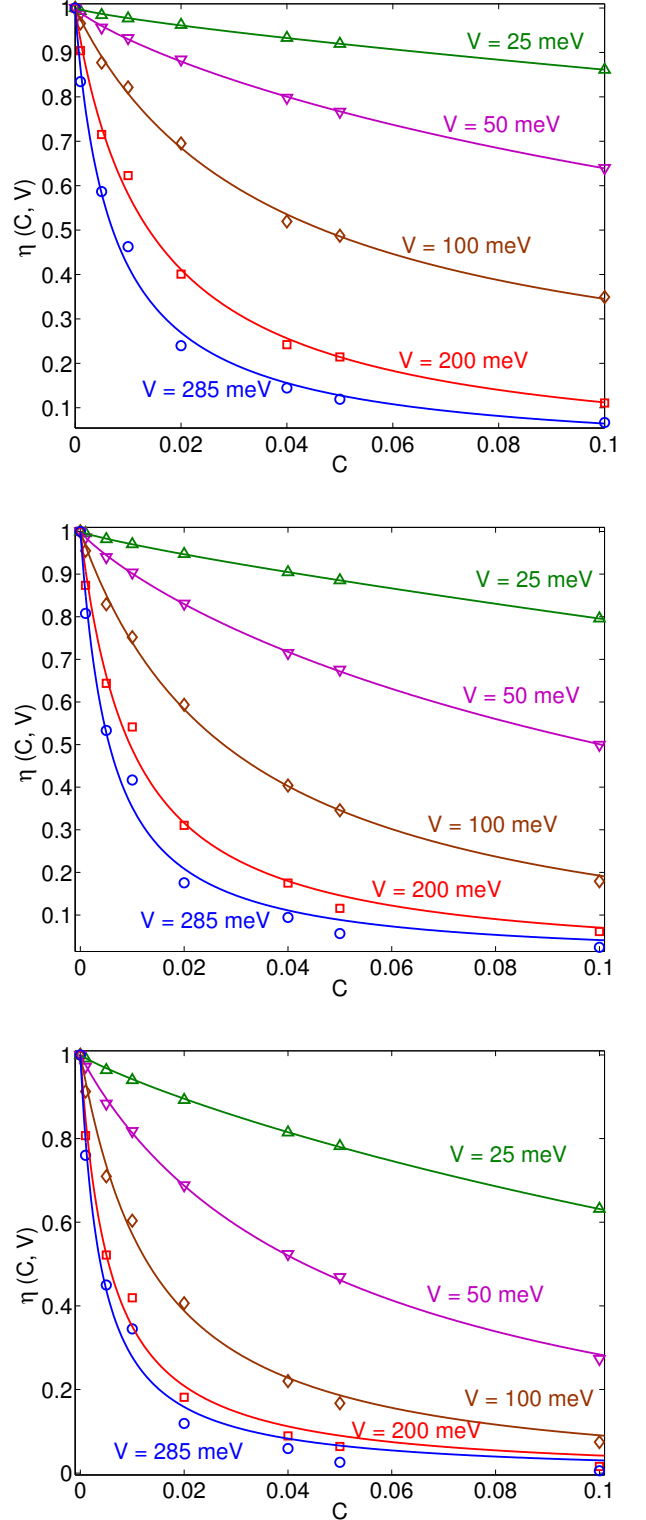

FIG. 12. Maximum value of T_{Jz} as a function of the impurity percentage for each value of the impurity potential $V = 50 \div 285$. For three values of the mass, $m = 0$ (top), 0.05 (middle), 0.1 (bottom).

	V (meV)	25	50	100	200	285
	A	1.09	0.26	0.046	0.017	0.0097
m=0	n	0.8	0.85	0.98	0.97	0.94
	Σ_0	0.51	0.23	0.17	0	0
	A	0.68	0.16	0.03	0.009	0.005
m=0.05	n	0.84	0.88	0.99	1.01	1.01
	Σ_0	0	0	0	0	0
	A	0.27	0.053	0.011	0.0053	0.0039
m=0.1	n	0.89	0.96	1.04	1.01	1.00
	Σ_0	0	0	0	0	0

TABLE I. Set of parameters that has been obtained by fitting the numerical results for Σ using Eq.(21).

(solid line), showing good agreement with the numerical data. We have plotted η instead of Σ, in order to avoid the divergence at $C = 0$. The values of the parameters can be found in Table I. From this Table, we appreciate that the residual Σ_0, is zero when the mass is different from zero, which points to this minimum permeability (conductivity) as to a property of massless particles. On the other hand, massive particles show a closer adherence to the Kozeny-Carman law, in the context of classical fluid dynamics[14,15], where no residual conductivity is observed at $C = 1$. Also, note that for low potential barriers, the exponent is around $n \sim 0.85$, while for intermediate and strong potentials it is near $n \sim 1$, i.e. the value it takes for classical fluid dynamics in a dilute disordered medium. Thus, for strong potentials, the classical analogy shows satisfactory results, while for intermediate and weak potentials, it presents deviations, typically of the order of 15%. Finally, we observe that the case $m = 0$ shows a significantly higher transmission than the corresponding data with $m > 0$, which is due to the higher momentum losses in the impurity region. It appears plausible to interpret the non-negligible surplus of relativistic conductivity, especially for the three cases with Fermi energy $E_F < V$, as an indirect manifestation of Klein tunneling.

V. CONCLUSIONS AND DISCUSSION

In this paper we have performed a numerical study of a relativistic Gaussian wave-packet propagating through a disordered medium, which we modeled as a set of randomly located potential barriers.

From the numerical results, we conclude that for high concentration of impurities, the wave packet presents higher losses in momentum. Furthermore, for a given impurity concentration, by increasing the potential of each impurity, we also find a loss of momentum. Systems with massive excitations are also studied, which can be of relevance to the case of gaped graphene samples. A non-zero mass is found to produce higher losses of momentum in the impurity region. The actual numerical values show that at high impurity concentration, $C = 0.05$, the wavepacket looses more than half of its momentum with barriers of 100 meV and up to 85% with $V = 285$ meV. At low concentrations, $C = 0.001$, however, the losses are much milder, going from about $5 - 20\%$, for $V = 100$ to 285 meV, respectively.

These data can be regrouped into an analytical expression, which bears a strong similarity with the permeability of porous media, as a function of the porosity. We have estimated the value of the conductivity from the transmission coefficient and fitted it by using the Carman-Kozeny law for porous media, relating the permeability with the concentration of impurities We have found that this analogy works pretty well for the massive case, which shows no residual conductivity and a scaling exponent pretty close to unity. On the other hand, the massless case shows a residual conductivity, which can possibly be related to the minimum conductivity of graphene. Moreover, for weak and intermediate potential strengths, the exponent is not unity, corresponding to a fractional Kozeny-Carman law. On the other hand, for strong potentials, the exponent 1 is recovered to a good accuracy, bringing the results closer to the analogy with classical fluids[27]. The applicability of this classical analogy indicates that, at least for the parameter set investigated in this paper, quantum tunneling is not the dominant transport mechanism, as compared to the semiclassical dynamics of the wave-function, which can turn around the obstacles in a similar way as a classical fluid would do. The results of this paper are expected to be amenable to experimental validation. For this purpose, samples of graphene with local chemical doping could be used[8,28]. In addition, for validating the results with massive particles, a substrate of SiC will also be required, in order to generate the gap due to the presence of particle mass. Finally, as a byproduct, we have introduced a new tool to model electronic transport in graphene, namely the quantum lattice Boltzmann method (QLB). QLB shares a remarkable computational efficiency, especially on parallel computers, and easy handling of complex geometries with its well-established classical LB counterpart. As a result, it is hoped and expected that the present model can make a contribution to the computational study of transport phenomena in graphene and other physical systems governed by the Dirac equation.

[*] silviapalpacelli@gmail.com

[†] mmendoza@ethz.ch

[‡] hjherrmann@ethz.ch

[§] succi@iac.cnr.it

[1] O. Klein, Zeitschrif Fr Physik a Hadrons and Nuclei, 53, 3-4, 157-165, (1929)

[2] K.S. Novoselov et al, Nature, 438, 197, (2005)

[3] K. Novoselov et al, Science, 306, 666, (2004).

[4] A. K. Geim and A,H. Mac Donald, Phys. Today, 35, (2007)

[5] E. Shuryak, Prog. Part. Nucl. Phys. 53, 273 (2004)

[6] M. Muller, J. Schmalian and L. Fritz, Phys. Rev. Lett. 103, 025301, (2009)

[7] M. Mendoza, H.J. Herrmann and S. Succi, Phys. Rev. Lett. 106, 156601, (2011).

[8] M. I. Katsnelson, K.S. Novoselov and A.K. Geim, Nat. Phys., 2, 620, (2006)

[9] C. Bai and X. Zhang, Phys. Rev. B, 76, 075430, (2007)

[10] E. Rossi et al, Phys. Rev. B, 81, 121408(R) (2010)

[11] S. Das Sarma, S. Adam, E.H. Hwang, and E. Rossi, Rev. Mod. Phys. 83, 407-470 (2011).

[12] S. Y. Zhou, G.-H. Gweon, A. V. Fedorov, P. N. First, W. A. de Heer, D.-H. Lee, F. Guinea, A. H. Castro Neto, and A. Lanzara, Nature Materials 6, 770 - 775 (2007).

[13] Vitor M. Pereira, Valeri N. Kotov, and A. H. Castro Neto, Phys. Rev. B 78, 085101 (2008).

[14] R.R. Rumer and P.A. Drinker, Proc. Am. Soc. Civil Eng., J. Hydraulic Div. 92 (HY5), pp. 155 (1966).

[15] J. Bear, Dynamics of Fluids in Porous Media, American Elsevier Publising Company (1972).

[16] S. Succi and R. Benzi, Physica D, 69, 327, (1993).

[17] P. Dellar and D. Lapitski, Phil. Trans. Roy. Soc. 369, 2155-2163, (2011).

[18] P. J. Dellar, D. Lapitski, S. Palpacelli and S. Succi, Phys. Rev. E 83, 046706, (2011).

[19] S. Palpacelli and S. Succi, Comm. in Comp. Phys, 4, 980, (2008).

[20] We wish to forestall any potential confusion, possibly arising from the denomination "Boltzmann" in the QLB framework. Here "Boltzmann" stems from the formal analogy between the *single-particle* Dirac equation and the Boltzmann equation of classical statistical mechanics. In this respect, QLB should be kept distinct from the quantum Boltzmann equation, typically used to address collective quantum transport phenomena.

[21] R. Benzi, S. Succi and M. Vergassola, Phys. Rep. 222, 145, (1992).

[22] V. B. Berestetskii, L. P. Pitaevskii, and E. Lifshitz, Quantum Electrodynamics (Butterworth-Heinemann, Oxford, 1982), 2nd ed.

[23] , J. Tworzydlo et al, Phys. Rev. B, 78, 235438, (2008)

[24] M. Bernaschi et al, Comput. Phys. Commun., 180, 1495, (2009), and, High Performance Computing, Networking, Storage and Analysis (SC), 2011 International Conference, 1-12, Issue 12-18 Nov. 2011, Gordon Bell Award Honorable Mention.

[25] Some references to technological applications can be found in A. H. Castro Neto, F. Guinea, N. M. R. Peres, K. S. Novoselov and A. K. Geim, Rev. Mod. Phys., 81, 1, 110 (2009).

[26] K. Nomura and A.H. Mac Donald, Phys. Rev. Lett. 98, 076602, (2007); V.M. Galitski et. al. Phys. Rev. B 76, 245405 (2007); E. Rossi and Das Sarma, Phys. Rev. Lett. 101, 166803 (2008); M. Polini et al., Phys. Rev. B 78, 115426 (2008)

[27] R. D'Agosta and M. Di Ventra, J. Phys.: Condens. Matter 18, 11059 (2006)

[28] K. S. Novoselov, A. K. Geim, S. V. Morozov, D. Jiang, Y. Zhang, S. V. Dubonos, I. V. Grigorieva, and A. A. Firsov, Science 22 306, 5696 pp. 666-669.